AUTHOR BIOGRAPHIES

Chang-Min Yuan, School of Civil Engineering & Transportation, South China University of Technology, Guangzhou, PR China

Jian Cai, School of Civil Engineering & Transportation, South China University of Technology, Guangzhou, PR China

Fangying Wang, Department of Civil Engineering, University of Nottingham, United Kingdom

An He, School of Civil Engineering & Transportation, South China University of Technology, Guangzhou, PR China

Bingquan He, Guangzhou Jishi Construction Group Co. LTD, Guangzhou, PR China

Qing-Jun Chen, School of Civil Engineering & Transportation, South China University of Technology, Guangzhou, PR China

Zhiliang Zuo, School of Civil Engineering & Transportation, South China University of Technology, Guangzhou, PR China

Testing of precast recycled aggregate concrete shear wall with pressed sleeve connection subjected to cyclic loading

Chang-Min Yuan [1,2], Jian Cai [1,2], Fangying Wang [3], An He [1,2,*], Bingquan He [4], Qing-Jun Chen [1,2], Zhiliang Zuo [1,2]

[1] School of Civil Engineering & Transportation, South China University of Technology, Guangzhou, PR China

[2] State Key Laboratory of Subtropical Building Science, South China University of Technology, Guangzhou, PR China

[3] Department of Civil Engineering, University of Nottingham, United Kingdom

[4] Guangzhou Jishi Construction Group Co. LTD, Guangzhou, PR China

[*] **Correspondence**: An He, E-mail: hean@scut.edu.cn, TEL: +86 (020)87114801

Abstract: The pressed sleeve connection is a new type of connection technique reported in China recently. To explore the possibility of combining the advantages of pressed sleeve connections and recycled aggregate concrete (RAC) in precast concrete, the seismic performance of precast shear walls with pressed sleeves and recycled fine aggregate (RFA) concrete was investigated through a thorough experimental programme. A total of seven precast shear wall specimens and one cast-in-situ specimen were fabricated and tested under lateral cyclic loading, considering the effects of the aspect ratio, the axial compression ratio, and the RFA content. The failure modes, hysteretic behaviour, bearing capacity, energy dissipation, stiffness and shear distortion of the specimens, as well as the strains of the steels, were reported and discussed. The test results demonstrated that the pressed sleeve connections were capable of transmitting both tensile and compressive forces between reinforcements, and the precast shear walls with pressed sleeve connections exhibited the same hysteresis behaviour, strengths, ductility coefficient and energy dissipation capacity as the cast-in-situ counterpart. Moreover, the seismic behaviour of the precast specimens with the RFA content of 30% was almost the same as those with natural aggregate concrete (NAC). The increase in the axial compression ratio and aspect ratio led to higher peak loads of the precast shear walls. Finally, existing design methods of ordinary reinforced concrete shear walls were evaluated for their application to the design of precast RFA concrete shear walls with pressed sleeves. Overall, the evaluation results revealed that the examined design methods offer generally accurate strength predictions for the proposed shear walls.

Keywords: Precast concrete; Pressed sleeve; Recycled aggregate concrete (RAC); Seismic performance; Shear wall

1 Introduction

The reinforced concrete (RC) shear walls are widely adopted for resisting lateral forces in high-rise buildings. Due to the development of construction industrialization, precast RC shear walls have received increasing attention from researchers and civil engineers as they accelerate the construction process compared with conventional cast-in-situ RC structures. In general, precast building connections are highly dependent on their stiffness, strength, and deformation capacity when it comes to seismic behaviour [1,2]. Thus, connections featuring high load-carrying capacities and simple detailing are required in practical engineering projects.

Unbonded post-tensioned connections are commonly used in precast RC shear walls. Experimental results of the post-tensioned precast shear walls under cyclic loading [3-5] have indicated that their seismic behaviour was similar to their cast-in-situ counterparts on behalf of strength and stiffness. Moreover, precast shear walls constructed of post-tensioned connections were equipped with replaceable connectors [6,7] and friction devices [8], in order to minimize the damage to concrete during an earthquake. The precast shear walls generally exhibited small residual deformations after unloading when subjected to reversed cyclic loads, as the post-tensioned tendons provide the self-centering capability [9]. However, the unbonded post-tensioned reinforcements may increase the compressive stress at the wall panels, resulting in excessive local bearing pressure at the interface of the precast walls and potential premature spalling of concrete. Moreover, a higher degree of construction quality and a more complex construction procedure are needed for these unbonded post-tensioned connections [10].

Grouted sleeve splicing connections, consisting of reinforcements joints and hollow cast iron cylinders, are gaining traction in the construction industry. Einea et al. [11] revealed that using steel tubes to confine the grout around the reinforcement could significantly strengthen the bond between spliced reinforcements, the lapped splice length can be as short as seven times the reinforcement diameter when appropriate grout and confinement were adopted.

Belleri and Riva [12] conducted cyclic loading tests on column-to-foundation subassemblies with grouted sleeve connection joints, and confirmed that the proposed connections are well suited for applications in earthquake-prone regions. An investigation by Peng et al. [13] explored the seismic performance of precast RC shear walls with the longitudinal reinforcements connected by mortar-sleeve connections. The precast shear walls showed similar failure modes compared with the cast-in-situ counterparts, and the mortar-sleeve splice effectively transferred the stresses in the longitudinal reinforcement. An investigation of seismic performance of a fully constructed precast RC shear wall structure with single-row grouted sleeves was carried out by Xu et al. [14,15], and demonstrated that the walls with the proposed connections exhibited a favourable seismic behaviour. Liu et al. [16] designed four prefabricated grouted sleeve columns with different reinforcement and stirrup ratios to assess their seismic performance. When compared with cast-in-situ columns, precast columns were comparable in ductility and lateral deformation capacity, but showed lower strengths. In summary, the grouted sleeve splices reduce the lap-splice length of reinforcements while effectively transmitting reinforcement stress. However, full compactness of the grouted mortar in the sleeve cylinder is not guaranteed due to the difficulty in accessing and monitoring the mortar within the cylinder, thereby increasing the risk of premature structural failure [17]. Additionally, the relatively high cost of the sleeves and the associated construction challenges impede its applications in practical engineering projects.

The pressed sleeve connections, characterising easy operation and fast construction, have been recently proposed to address the disadvantages of the above-mentioned precast connections, as a new type of connection technique in China. The experimental investigations onto the seismic performance of structural members with pressed sleeves [18-20] have recently been reported in China, which showed that the connection features favourable seismic performance through thoughtful design.

On the other hand, resource and carbon dioxide emission constraints have prompted using recycled aggregate concrete (RAC) in the construction industry. Experimental studies have shown that the material properties of RAC are slightly weaker than those of conventional natural aggregate concrete (NAC), owing to the randomness and diversity in the material characteristics of the recycled coarse aggregate (RCA) or recycled fine aggregate (RFA) to a certain extent [21-24]. Nevertheless, substantial experimental studies on the seismic performance of RAC structural members have indicated that the RAC structural members could be comparable to their NAC counterparts in terms of seismic behaviour through reasonable design [25]; this reveals a potential application of RAC in practical construction engineering. However, the application of RAC in precast structures, particularly for precast shear walls, is seldom explored, given the fact that the majority of the previous research focused on cast-in-situ RAC structures.

The current study presents a precast RFA concrete shear wall with the pressed sleeves at the splice joints, combining the advantages of RAC and pressed sleeve connections, in order to significantly minimize the emissions of carbon dioxide due to the fabrication of precast structures. The specifications for the pressed sleeve connection in the precast wall are depicted in Figure 1, the reinforcements from both the upper and lower precast walls are connected by the pressed sleeves with post-cast concrete infilled in the connection region. Figure 2 presents the procedure of using the pressed sleeve to connect two separated bars splices. In order to produce plastic deformation on the steel sleeve, hydraulic moulds are applied. This results in a highly firm contact between the sleeve and the bar splice, which is attributed from interfacial friction and mechanical interlocking. Considering the space limitations for the press machine and achieving on-site construction efficiency, half of the reinforcements were connected by pressed sleeves and the rest were connected by lap-splices with post-cast concrete infilled in the connection region, as shown in Figure 3. Seven precast shear wall specimens with the pressed sleeve connections and one reference cast-in-situ specimen, were fabricated and evaluated under lateral cyclic loading programme, to examine the seismic behaviour of the suggested shear walls. The influences of the aspect ratio, the axial compression ratio, and the RFA content in concrete of the member were considered in the experiments. The failure modes, hysteresis behaviour, strength, deformation of the shear walls, and strains of the steels were discussed. Finally, the existing design methods for ordinary RC shear walls, as specified in the Chinese code JGJ 3-2010 [26], were adopted to assess their applicability to the design of precast RFA concrete shear walls with pressed sleeve connections.

2 EXPERIMENT PROGRAMME

2.1 Details of specimens

A total of eight shear wall specimens were prepared in the laboratory. The overall sizes of all the specimens were predefined to be approximately 1/2 of the full-scale real structural elements, due to the size limitation of the test setup. The geometric dimensions of the precast specimens are displayed in Figure 3. Each specimen consists of a concrete foundation (with a cross-section of 500 mm×500 mm), a concrete wall (with the thickness being 120 mm), and a concrete loading girder (with a cross-section of 250 mm×250 mm), in which the wall portion included a precast panel (with a cross-section of 960 mm×120 mm), a horizontal connection composed of several pressed sleeves and the post-cast concrete, and the post-cast boundary members (with their cross-sections being 240 mm×120 mm). The resulting cross-section dimensions of the precast walls after casting concrete in the boundary members were 1440 mm×120 mm. The main parameters of the specimens are listed in Table 1, in which ω is the content of RFA in RAC, H_p and H are respectively the heights of the precast panel and the shear wall, and N_d is the applied axial compressive load. The axial compression ratio (n_d) and the aspect ratio (λ) were respectively calculated by Eq. (1) and Eq. (2) [27], where A is the cross-section area of the shear wall, H_0 is the effective height of the shear wall, taken as the distance from the loading point to the bottom of the wall, h_w is the cross-section width of the shear wall taken as 1440 mm for all the specimens, and f_c is the axial compressive strength of concrete in the connection. Each specimen's label is preceded by the letters 'SW' (for cast-in-situ shear wall) or 'PW' (for precast shear wall), then the aspect ratio, axial compression ratio and the content of RFA in RAC.

$$n_{\mathrm{d}} = \frac{N_{\mathrm{d}}}{f_{\mathrm{c}} A} \tag{1}$$

$$\lambda = \frac{H_0}{h_{\mathrm{w}}} \tag{2}$$

The reinforcement layout for the specimens are shown in Figure 4. A total of fourteen longitudinal reinforcements with the diameter of 12 mm were arranged in the wall panel, half of the reinforcements were connected by pressed sleeves and the rest were connected by lap-splices. U-shaped hoops with the diameter of 8 mm were anchored into the precast wall panel and adopted as stirrups of the boundary members. The boundary members were fabricated by the lapped longitudinal reinforcements with a diameter of 12 mm and post-cast concrete, considering the construction convenience of connecting the adjacent structural members (such as other walls and beams) in practical engineering.

The assembly process of the specimens is indicated in Figure 5. The wall panel with a loading girder and the foundation were prefabricated in the factory. After that their longitudinal reinforcements were aligned, and connected through pressed sleeves and lap-splice connections. The construction of the pressed sleeves using the hydraulic jack and the hydraulic moulds is shown in Figure 6. Finally, the boundary members and the connection region were cast with RAC.

2.2 Materials

Recycled fine aggregate (RFA) was used to fabricate the precast shear walls and the post-cast concrete. According to the Chinese code GB/T 25176-2010 [28], the material characteristics of the RFA were measured based on and presented in Table 2. The RAC was designed based on NAC with Grade C40 [27], with their mix proportions determined according to JGJ/T 240-2011 [29] and listed in Table 3. For each type of concrete, three 150 mm concrete cubes were set aside and allowed to cure under the same conditions as the wall specimens to determine their actual cubic compressive strengths f_{cu} at the time of cyclic testing. Table 4 lists the average measured values of f_{cu} for all the concrete types. The axial compression strength f_{c}, the axial tension strength f_{t} and the elastic modulus E_{c} of concrete were then calculated by Eqs. (3)–(6) [27,30] and listed in Table 4.

$$f_{\mathrm{c}} = 0.76 f_{\mathrm{cu}} \tag{3}$$

$$f_{\mathrm{t}} = 0.395 f_{\mathrm{cu}}^{0.55} \tag{4}$$

$$E_{\mathrm{c}} = \frac{10^5}{2.2 + \dfrac{34.7}{f_{\mathrm{cu}}}} \text{ (for NAC)} \tag{5}$$

$$E_{\mathrm{c}} = \frac{10^5}{2.8 + \dfrac{40.1}{f_{\mathrm{cu}}}} \text{ (for RAC)} \tag{6}$$

Grade HRB400 steel [27] was used for all the reinforcements of the specimens. Tensile coupon tests were carried out to derive the material properties of the reinforcements. Table 5 collects the measured yield strength f_{y}, ultimate strength f_{u} and Young's modulus E_{s}. The pressed sleeves were manufactured using Type 20 carbon steel [31], and supplied by Ji'nan Hegui Machinery Equipment Co. LTD. The geometric dimensions of the pressed sleeves are reported in Table 6. Tensile tests on the pressed sleeve connections were also conducted following the test procedures in JGJ 107-2016 [32], with the test setup displayed in Figure 7.

The failure modes of the pressed sleeve connections were generally characterized by the fracture of the connected reinforcement, while the pressed sleeve remained intact, as shown in Figure 8(a). Figure 8(b) compares the tensile force–displacement curves of the pure reinforcements and the sleeve connections, which reveals that the sleeve connections generally exhibited similar strengths with enhanced deformation capacity when compared to the reinforcements.

2.3 Experiment setup and measurements

Figure 9 depicts the test setup for the shear wall specimens. The foundation of the specimen was fixed by the hydraulic jack and the vertical tie rods onto the floor. The axial compressive load was delivered to the predefined value initially by using a hydraulic jack with rolling support, and remained unchanged during the subsequent cyclic horizontal loading. Due to the capacity limit, two 1000 kN capacity MTS actuators were used to apply horizontal loads to the specimen through the rigid loading girder. The horizontal loads were applied by displacement control through drift angles, following the cyclic loading spectrum shown in Figure 10. The drift angle was defined by Eq. (7), where $\mathit{\Delta}$ is the horizontal displacement at the loading point. A set of drift angle amplitude, including 1/1000, 1/800, 1/500, 1/400, 1/250, 1/200, 1/135, 1/100, and 1/75, were utilized for the whole horizontal loading, with each cycle repeated twice. The experiments were terminated when the axial load could not be kept constant or the horizontal bearing capacity of the specimen had dropped below 85% of its maximum value.

$$\theta = \frac{\mathit{\Delta}}{H_0} \tag{7}$$

The instrumentations of the cyclic loading test are depicted in Figure 9. The axial compression force was captured by the load sensor of the jack, and the horizontal load was recorded by MTS actuator systems. A pair of linear variable differential transducers (LVDTs)

D1 and D2 were positioned diagonally on the back side of the wall to record its shear deformation. The horizontal displacement at the loading point was taken as the average value from LVDTs D3 (front side) and D4 (back side). Strain gauges were affixed on the reinforcements and the pressed sleeves, with their positions marked in Figure 11.

3 Test results and discussion

3.1 Failure modes

All the specimens failed in similar manner, with crack patterns shown in Figure 12. Regarding the precast specimen PW-1.1-0.33-30%, small horizontal cracks appeared at the splice joint at the drift angle of 1/1000 and continued to develop when the drift ratio increased to 1/800. The tensile reinforcement of the specimen yielded at the drift ratio of 1/400, and the shear cracks (approximately 45° from the horizontal line) began to appear on the tensile side of the wall. When the drift angle increased to 1/250, the bending and shear cracks penetrated to the mid-height of the wall. At the drift angle of 1/135, concrete spalling occurred in the bottom of the compressive boundary member, and the specimen reached its maximum lateral strengths of 907.0 kN and 894.3 kN in positive and negative loading directions, respectively. When the drift angle increased to 1/100, the specimen failed to bear the axial compression load and showed a flexure-compression failure mode upon completion of testing. There were no penetrating horizontal fractures between the splice joint and the precast wall, indicating that sliding deformation was insignificant when the specimen failed.

The experimental observations of the cast-in-situ specimen SW-1.1-0.33-30% were similar to those of specimen PW-1.1-0.33-30%, except that several vertical compressive cracks were found in the wall panel, owing to the concentration of axial compression force in the middle of the loading girder. Specimen PW-1.4-0.33-30% with λ=1.4 behaved similarly to specimen PW-1.1-0.33-30% (λ=1.1), with extensive bending cracks formed and evenly distributed on the wall. Specimen PW-0.9-0.33-30% with λ=0.9 was characterized by extensive shear cracks and failed by a flexure-shear mode. For specimen PW-1.1-0.45-30% with a higher compression ratio of 0.45, the flexure cracks developed more slowly, and the severe spalling of concrete at the bottom of the boundary members was observed. On the contrary, flexure cracks appeared earlier and developed faster on specimen PW-1.1-0.20-30% with nd=0.20; this is due to the fact that the smaller axial compression force could not counteract the tensile force in the concrete fibres at the tensile boundary member. The failure process of the specimens PW-1.1-0.33-0 and PW-1.1-0.33-70% were almost identical to the standard specimen PW-1.1-0.33-30%, indicating that use of RFA concrete did not have an unfavourable influence on the failure modes of the specimens.

In addition, the post-cast concrete at the connection region was removed upon testing to examine the condition of pressed sleeves, as a typical photo from specimen PW-1.1-0.33-30% shown in Figure 13, where they were intact and stably connected with the reinforcements.

3.2 Hysteresis curves

The lateral force–drift angle (P–θ) hysteresis curves for all specimens are displayed in Figure 14, together with the lateral force–displacement (P–Δ) hysteresis curves. In general, all the specimens entered into the elastic state without noticeable residual deformation when unloading within the drift angles of 1/800, indicating a linear structural response of the precast walls. The hysteretic curves generally became full with obvious residual deformation when unloading as the drift angle increased to 1/400~1/250. In this stage, the strengths of the specimens kept growing with accumulated residual deformation, leading to an expansion of the closed area of the hysteresis curves. After the maximum lateral loads were attained, the pinching effect became more evident in hysteresis loops because of the slippage of the longitudinal reinforcements, while the lateral stiffness and the lateral bearing capacity were reduced due to the damage accumulation.

As displayed in Figs. 14(a) and 14(b), the precast shear wall PW-1.1-0.33-30% had similar hysteresis curves to the reference cast-in-situ specimen SW-1.1-0.33-30%. As shown in Figs. 14(b), 14(e), and 14(f), the increase of the axial compression load led to a reduction in the deformation capacity since the drift angles at the final loading stages were 1/75, 1/100 and 1/200 for PW-1.1-0.20-30%, PW-1.1-0.33-30% and PW-1.1-0.45-30%, respectively. In addition, there was no considerable variation in the form of the hysteretic curves for specimens with various RFA content and aspect ratios, indicating that these factors had insignificant influence on the hysteresis curves.

3.3 Skeleton curves

The lateral force–drift angle (P–θ) skeleton curves, taken as the envelope of each hysteretic curve, are displayed in Figure 15. Table 7 lists the peak load P_m, the drift angle at the peak load θ_m, the ultimate load P_u, and the drift angle at the ultimate load θ_u determined from the P–θ skeleton curves. Note that θ_u is defined as the drift angle at 0.85P_m in the post-peak branch of the skeleton curve or the maximum drift angle during cyclic loading tests for those severely damaged specimens incapable of reaching 0.85P_m.

It can be observed from Figure 15(a) and Table 7 that the skeleton curve, the load-carrying capacity and the ultimate deformation of the precast specimen PW-1.1-0.33-30% and the cast-in-situ counterpart SW-1.1-0.33-30% were similar. Thus, the precast wall with pressed sleeves can be seen as equivalent to the cast-in-situ one. Comparing specimens PW-1.1-0.33-30%, PW-0.9-0.33-30% and PW-1.4-0.33-30% with different aspect ratios, it is found in Figure 15(b) and Table 7 that the bearing capacity of the specimen with the aspect ratio of 0.9 was about 12.6% and 30.2% greater than those of the specimens with λ=1.1 and λ=1.4, respectively, which means the bearing capacity rose gradually with the decrease of aspect ratio. As evidently shown in Figure 15(c) and Table 7, the increase in the axial compression ratio significantly increased the lateral bearing capacity of the shear wall specimens. The average lateral bearing capacities for specimens PW-1.1-0.45-30% (with n_d=0.45) and PW-1.1-0.33-30% (with n_d=0.33) increased by 14.0% and 9.5% when compared with specimen PW-1.1-0.20-30% (with n_d=0.20). However, the higher axial compression ratio had an adverse effect on the ultimate deformation capacities of the specimens. For the specimen series with different RFA content presented in Figure 15(d), it was found that specimen PW-1.1-0.33-30% with the RFA content of 30% had identical bearing capacities to specimen PW-1.1-0.33-0 with natural aggregate concrete. However, the average bearing capacity of specimen PW-1.1-0.33-70% with the RFA content of 70% decreased by 22.0% when compared to those of specimen PW-1.1-0.33-0.

3.4 Ductility

The ductility coefficient (μ) is a quantitative measure of the post-peak deformation capacity, and can be determined by Eq. (8), where the yield drift angle θ_y of each specimen was determined using the method proposed by Park [33].

$$\mu = \frac{\theta_u}{\theta_y} \tag{8}$$

Table 7 listed the yield load P_y, the drift angle at the yield load θ_y, as well as the ductility coefficients. The drift angle at the ultimate load varied from 1/195 to 1/81, while the ductility coefficients μ were in the range from 2.2 to 4.4, which demonstrated that the specimens exhibited favourable deformation capacity during the post-peak stage. The precast shear wall had almost the same ductility coefficients to the cast-in-situ counterpart. The increase in the axial compression ratio and the RFA content may lead to an adverse impact on the ductility, as the concrete is more fragile in the case of high axial compression ratio, resulting in the premature failure of concrete due to crushing and spalling.

3.5 Stiffness degradation

The secant stiffness–drift angle curves for the specimens are shown in Figure 16, in which the secant stiffness K_j is defined by Eq. (9) [34], where $+P_{i,j}$ and $-P_{i,j}$ are the peak loads corresponding to the positive and negative direction in the *i*th loading cycle at the *j*th drift angle stage, respectively; $+\Delta_{i,j}$ and $-\Delta_{i,j}$ are the displacements associated with $+P_{i,j}$ and $-P_{i,j}$, respectively; *m* stands for the number of loading cycles.

$$K_j = \frac{\sum_{i=1}^{m} \left|+P_{i,j}\right| + \left|-P_{i,j}\right|}{\sum_{i=1}^{m} \left|+\Delta_{i,j}\right| + \left|-\Delta_{i,j}\right|} \tag{9}$$

As shown in Figs. 16(a)–16(d), the stiffness of the specimens reduced in a non-linear pattern as the drift angle raised. As displayed in Figure 16(a), the degradation curves of the precast specimen were identical to those of the cast-in-situ counterpart, indicating that the precast specimen had comparable stiffness degradation properties with the cast-in-situ one. As shown in Figure 16(b), specimens with a smaller aspect ratio had greater stiffness and steeper stiffness degradation. In contrast, the stiffness and stiffness degradation were insensitive to the variation of the axial compression ratio, as evident in Figure 16(c). As displayed in Figure 16(d), specimen PW-1.1-0.33-30% exhibited similar stiffness degradation curves to its counterpart with natural aggregate concrete, while those of the specimen with 70% RFA content were significantly lower.

3.6 Energy consumption

In this section, the cumulative energy dissipation as well as the equivalent viscous damping factor of the specimens during cyclic loading were discussed. The cumulative energy dissipation $\sum E$ is denoted as the total area encompassed by each hysteresis loop (see the shaded part in Figure 17). The cumulative energy dissipations for each specimen series are plotted against the cycle numbers and shown in Figure 18, in which an overall rising trend of the energy dissipation was observed. As displayed in Figure 18(a), the energy dissipation capacity of the precast specimen was almost equivalent to that of the cast-in-situ specimen during the whole loading process. The specimens with smaller aspect ratios or higher axial compression ratios were favourable to the dissipated energy under the same drift angle, as evident in Figs. 18(b) and 18(c). As shown in Figure 18(d), specimen PW-1.1-0.33-30% with the 30% RFA content had almost the same energy consumption capacity as specimen PW-1.1-0.33-0 with NAC. However, the energy consumption capacity of the specimen PW-1.1-0.33-70% with the RFA content of 70% was significantly reduced.

The equivalent viscous damping factor ξ_{eq} is further adopted to evaluate the energy dissipation capacity of each specimen. The equivalent viscous damping factor is calculated by Eq. (10) [34], where S_{ABC} and S_{ACD} are respectively the shaded part enclosed by the hysteresis curves, and S_{OBE} and S_{ODF} are the areas of the two triangles bounded by the hysteresis curves in Figure 17. The equivalent viscous damping factors for each specimen series were plotted against the loading cycle numbers and shown in Figure 19. In general, the equivalent viscous damping factors ranged from 0.05 and 0.15 prior to severe damage of the specimens. Both precast and cast-in-situ specimens had exactly similar factors as the loading cycle numbers increased. Specimen PW-0.9-0.33-30% with the aspect ratio of 0.9 had higher values of ξ_{eq} during the cyclic loading process when compared to its counterparts PW-1.1-0.33-30% and PW-1.4-0.33-30%. Moreover, the effect of the RFA content and the axial compression ratio on the equivalent viscous damping factor was limited, as evident in Figs. 19(c) and 19(d).

$$\xi_{eq} = \frac{1}{2\pi} \cdot \frac{S_{ABC} + S_{ACD}}{S_{OBE} + S_{ODF}} \tag{10}$$

3.7 Shear distortion

The total deformation of the shear wall consists of bending deformation and shear distortion at the loading point. The shear distortion Δ_s is defined as the deformation induced by the shear force, and can be calculated by Eq. (11) [35] using the schematic diagram depicted in Figure 20, where d_1 and d_2 are the original diagonal lengths, respectively, D_1 and D_2 are respectively the elongation or shortening measured by the LVDTs D1 and D2 (see Figure 9(b)), and h' is the height of the calculated section for shear deformation.

$$\Delta_s = \frac{1}{2}\left|\sqrt{(d_1+D_1)^2-h'^2}-\sqrt{(d_2+D_2)^2-h'^2}\right| \tag{11}$$

Figure 21 depicts the ratios of shear distortion to total deformation for each specimen series plotted against drift angles. It is revealed that the proportion of shear distortion of all the specimens steadily developed with the increase of drift angles. The precast specimen PW-1.1-0.33-30% possessed a similar maximum shear distortion ratio equal to approximately 0.5 as the reference cast-in-situ one. The shear distortion ratio significantly increased with the decrease in aspect ratio, reaching up to 0.8 for specimen PW-0.9-0.33-30%. In addition, the variation of the axial compression and RFA content were found to be insensitive to the shear distortion ratio.

3.8 Strain of reinforcements

The stresses of the longitudinal and horizontal reinforcements, as well as the pressed sleeves, are discussed in this section. Figures 22(a) and 22(d) show typical stresses of the longitudinal and horizontal reinforcements at the bottom of the shear wall for specimen PW-1.1-0.33-30% plotted against the drift angles. It is worth noting that the positive and negative values stand for tensile and compressive strains, respectively. It can be seen from Figs. 22(a) and 22(b) that the longitudinal reinforcements in the boundary members were subjected to repeatedly tensile and compressive strains during cyclic loadings, and they reached their yield strain near the drift angle of 1/400. The horizontal reinforcements at the bottom of the shear walls did not reach their yield strains, as evident in Figure 22(c). This revealed that the horizontal reinforcements did not bear a comparable amount of load during the whole loading. Regarding specimen PW-0.9-0.33-30%, the horizontal reinforcements in the precast wall panel reached their yield strains at the drift angle of 1/250, as shown in Figure 23; this showed good agreement with the experimental findings that the specimen eventually failed by a flexure-shear mode.

In Figure 24, the strains of the pressed sleeves and the associated longitudinal reinforcements are shown versus the drift angles. It can be seen that the compressive and tensile strains of both pressed sleeves and the associated reinforcements were almost in the same trend, revealing a reasonable load transfer capacity during the experiment. The tensile strains of the reinforcement below the sleeve (i.e., strain gauges V4 and V5) are significantly greater than those of the reinforcement above the sleeve (i.e., strain gauges V9, V10, V12 and V13), while the compressive strains of the reinforcement below the sleeve were slightly higher. This is mainly due to the interaction effect of the concrete at the upper and lower ends of the sleeve. Besides, the sleeves (measured by strain gauges V11 and V14) did not reach their yield strains, since the cross-section area of the sleeves was larger than the reinforcements.

4 Design of the precast shear walls

4.1 General

The experimental results presented in Section 3 have demonstrated that the precast shear walls with pressed sleeve connections behaved in a similar manner to the cast-in-situ ones. Thus, the existing design rules for normal RC shear walls, as given in the Chinese code JGJ 3-2010 [26], were assessed for their applicability to the design of precast shear walls with pressed sleeve connections. In the following subsections, the calculations of the sliding strength, flexural strength and shear strength are fully described. The strength predictions were then compared against the experimental results, with the mean ratio of the predicted strengths to the experimental peak loads and the corresponding COV listed in Table 8.

4.2 Sliding strengths

For precast shear walls with horizontal construction joints at the bottom, slippage may occur at the interface between the precast wall and the foundation. The sliding strength V_{sl} at the horizontal construction joints is calculated by Eq. (12), where f_y and A_s are the measured yield strength and total cross-section area of longitudinal reinforcements, respectively, and N_d is the applied axial compressive load.

$$V_{\mathrm{sl}} = 0.6 f_{\mathrm{y}} A_{\mathrm{s}} + 0.8 N_{\mathrm{d}} \tag{12}$$

The sliding strength predictions V_{sl} determined by Eq. (12) were compared against the experimental peak loads and summarized in Table 8, in which the predictions were much greater than the test results. This is consistent with the test observation, in which the precast specimens eventually failed by either flexure-compression or flexure-shear modes without significant sliding.

4.3 Flexural strengths

Based on the experiment results in this study, there is a trend that the precast recycled aggregate concrete shear walls with pressed sleeves were failed in flexure-compression or flexure-shear modes. Therefore, the design method for flexural strengths of normal shear walls, as specified in JGJ 3-2010 [26], was employed herein. The schematic diagram is depicted in Figure 25, which is determined based on both force and moment equilibrium with the plane section assumption. Note that the tensile reinforcements located outside 1.5 times the concrete compressive block, as well as the reinforcements in the compressive boundary member, were assumed to be yielded. The force and moment equilibrium for the bottom section of the precast wall are respectively given by Eqs. (13) and (14), where x is the relative depth of the compressive area, α_1 is the coefficient and taken as 1.0, f_c is the axial compression strength of concrete, b and h_w are the thickness and width of the wall section respectively, f'_y and f_y are respectively the yield strengths of the compressive and tensile reinforcements in boundary members, A_s and A'_s are respectively the total cross-section area of reinforcements in the tensile and compressive boundary member, A_{sw} and f_{yw} are respectively the total cross-section area and yield strength of the longitudinal reinforcements in wall panel, h_{w0} is the distance from the extreme compressive fibre to the centroid of the tensile reinforcements in the boundary member, and a'_s is the distance from the extreme compressive fibre to the centroid of the reinforcements in the compressive boundary member.

$$N_d = \alpha_1 f_c bx + f'_y A'_s - f_y A_s - f_{yw} \frac{A_{sw}}{h_w}(h_w - 1.5x) \tag{13}$$

$$M = f_{yw} \frac{A_{sw}}{h_w}(h_w - 1.5x)\left(\frac{h_w}{2} + \frac{x}{4}\right) + N\left(\frac{h_w}{2} - \frac{x}{2}\right) + f_y A_s (h_{w0} - a'_s) \tag{14}$$

Upon determination of the ultimate moment capacities of the precast shear walls by Eqs. (13) and (14), the flexural strength of the precast wall P_f can be calculated by Eq. (15). Table 8 summarizes the flexural strength prediction of each precast shear wall specimen. The mean ratio of the predicted to test results P_f/P_{avg} and the corresponding COV are equal to 0.92 and 0.05, respectively. It confirms that the design methods given in JGJ 3-2010 [26] can be generally safely applied to precast shear walls with pressed connections failed by flexure-compression or flexure-shear.

$$P_f = M / H_0 \tag{15}$$

4.4 Shear strengths

The design method for the shear strength of RC shear walls with the aspect ratio smaller than 1.5, as given by JGJ 3-2010 [26], considers the beneficial effect of axial compressive load on the shear strength of shear walls. The formula is given in Eq. (16), where f_t is the tensile strength of concrete, N is the axial compressive load and is limited to $0.2 f_c b h_w$, f_{yw} is the yield stress of horizontal web reinforcements, s_v is the spacing of the horizontal reinforcements, and A_W and A are the web and total cross-section area of the shear wall, respectively.

$$V_{\mathrm{s}}=0.4f_{\mathrm{t}}bh_{\mathrm{w0}}+0.1N\frac{A_{\mathrm{W}}}{A}+0.8f_{\mathrm{yw}}\frac{A_{\mathrm{sh}}}{s_{\mathrm{v}}}h_{0} \tag{16}$$

The shear strengths of each precast wall with pressed connections are calculated by Eq. (16) and listed in Table 8. It is indicated that the predictions were conservative when compared against the test strengths except for specimen PW-0.9-0.33-30% failed by the flexure-shear mode. This is consistent with the experimental observations, where specimen PW-0.9-0.33-30% was characterized by many penetrating shear cracks when the specimen failed.

5 Conclusions

A precast RFA concrete shear wall with pressed sleeves at the splice joints was proposed in this paper. Lateral cyclic loading tests were conducted on seven precast shear wall specimens with the pressed sleeve connections, as well as one reference cast-in-situ specimen, to examine their seismic performance. Based on the results and discussion of the research, the following conclusions can be obtained:

(1) The pressed sleeve connections were capable of transmitting both tensile and compressive force between reinforcements. During cyclic loading tests, the precast shear walls with pressed sleeve connections had almost the same hysteresis behaviour, strengths, ductility coefficient and energy dissipation capacity as the cast-in-situ ones, with the pressed sleeves kept intact and stably connected with the reinforcements. Thus, the precast shear wall connected by pressed sleeves could be considered equal to the cast-in-situ counterpart.

(2) Within the range of parameters selected in this study, the seismic performance of the precast specimens with an RFA content of 30% was almost the same as that of the precast specimens with natural aggregate concrete, while the behaviour of the specimen with a higher RFA content became worse.

(3) Similar to the cast-in-situ shear wall, the aspect ratio had a significant impact on the seismic behaviour of the precast ones. The bearing capacity of the specimen with the aspect

ratio of 0.9 was about 12.6% and 30.2% greater than those of the specimens with λ=1.1 and λ=1.4, respectively. With the decrease in the aspect ratio, the precast shear wall specimens exhibited greater stiffness, steeper stiffness degradation and higher dissipated energy.

(4) The drift angles at the yield loads of the precast specimens ranged from 1/463 to 1/267, with their ultimate loads in the range between 1/195 and 1/81. The equivalent viscous damping factor ranged from 0.05 to 0.3 prior to severe damage of the specimens, which demonstrated that the proposed precast shear walls had a desirable deformation and energy consumption capability.

(5) The existing design rules JGJ 3-2010 [26] were found to be applicable for predicting the strengths of the proposed precast RFA concrete shear walls with pressed sleeve connections with a high design accuracy.

ACKNOWLEDGEMENTS

This work was supported by National Natural Science Foundation of China (Grant No. 52178139), Guangdong Provincial Natural Science Foundation of China (Grant No. 2022A1515011115), Youth Talent Support Programme of Guangdong Provincial Association for Science and Technology (Grant No. SKXRC202307), and Science and Technology Planning Project of Guangzhou Municipal Construction (Grant No. [2021]-KJ004; [2021]-KJ021; [2021]-KJ036; [2021]-KJ037).

REFERENCES

1 M.J.N. Priestley, Overview of PRESSS research program, PCI J. 36 (4) (1991) 50-57, http://doi.org/10.15554/pcij.07011991.50.57

2 Y. Kurama, S. Sritharan, R.B. Fleischman, et al., Seismic-resistant precast concrete structures: state of the art, J. Struct. Eng. 144 (4) (2018) 03118001, https://doi.org/10.1061/(ASCE)ST.1943-541X.0001972

3 Y. Kurama, S. Pessiki, R. Sause, et al., Seismic behavior and design of unbonded post-tensioned precast concrete walls. PCI J. 44 (3) (1999) 72-89, https://doi.org/10.15554/pcij.05011999.72.89

4 Y. Kurama, R. Sause, S. Pessiki, et al., Lateral load behavior and seismic design of unbonded post-tensioned precast concrete walls. ACI STRUCT. J. 96 (4) (1999) 622-632, https://doi.org/10.14359/700

5 Z. Zhu, Z. Guo, Experimental study on emulative hybrid precast concrete shear walls, KSCE J. Civ. Eng. 21 (1) (2017) 329-338, http://doi.org/10.1007/s12205-016-0620-4

6 S. Sritharan, S. Aaleti, R.S. Henry, et al., Precast concrete wall with end columns (PreWEC) for earthquake resistant design, Earthq. Eng. Struct. D. 44 (12) (2015) 2075-2092, http://doi.org/10.1002/eqe.2576

7 K.M. Twigden, S. Sritharan, R.S. Henry, Cyclic testing of unbonded post-tensioned concrete wall systems with and without supplemental damping, Eng. Struct. 140 (2017) 406-420, http://doi.org/10.1016/j.engstruct.2017.02.008

8 G. Xu, A. Li, Seismic performance and design approach of unbonded post-tensioned precast sandwich wall structures with friction devices, Eng. Struct. 204 (2020) 110037, http://doi.org/10.1016/j.engstruct.2019.110037

9 F. Perez, S. Pessiki, R. Sause, Experimental Lateral Load Response of Unbonded Post-Tensioned Precast Concrete Walls. ACI STRUCT. J. 110 (6) (2013) 1045-1056, http://doi.org/10.14359/51686159

10 Q. Yan, T. Chen, Z. Xie, Seismic experimental study on a precast concrete beam-column connection with grout sleeves, Eng. Struct. 155 (2018) 330-344, http://doi.org/10.1016/j.engstruct.2017.09.027.

11 A. EINEA, T. YAMANE, M.K. TADROS, Grout-filled pipe splices for precast concrete construction, PCI J. 40 (1) (1995) 82-93, http://doi.org/10.15554/pcij.01011995.82.93

12 A. Belleri, P. Riva, Seismic performance and retrofit of precast concrete grouted sleeve connections, PCI J. 57 (1) (2012) 97-109, https://doi.org/10.15554/pcij.01012012.97.109

13 Y. Peng, J. Qian, Y. Wang, Cyclic performance of precast concrete shear walls with a mortar–sleeve connection for longitudinal steel bars, Mater. Struct. 49 (6) (2016) 2455-2469, http://doi.org/10.1617/s11527-015-0660-0

14 G. Xu, Z. Wang, B. Wu, et al., Seismic performance of precast shear wall with sleeves connection based on experimental and numerical studies, Eng. Struct. 150 (2017) 346-358, http://doi.org/10.1016/j.engstruct.2017.06.026

15 G. Xu, Z. Wang, B. Wu, et al., Pseudodynamic tests with substructuring of a full-scale precast box-modularized structure made of reinforced concrete shear walls, The Structural Design of Tall and Special Buildings 26 (16) (2017) e1354, http://doi.org/10.1002/tal.1354

16 Y. Liu, B. Zhou, J. Cai, et al., Experimental study on seismic behavior of precast concrete column with grouted sleeve connections considering ratios of longitudinal reinforcement and stirrups, B. Earthq. Eng. 16 (12) (2018) 6077-6104, http://doi.org/10.1007/s10518-018-0414-9

17 F. Xu, K. Wang, S. Wang, et al., Experimental bond behavior of deformed rebars in half-grouted sleeve connections with insufficient grouting defect, Constr. Build. Mater. 185 (2018) 264-274, http://doi.org/10.1016/j.conbuildmat.2018.07.050

18 N. Li, J. Qian, L. Ye, et al., Tests on seismic behavior of precast RC shear walls with vertical rebar splicing by pressed sleeve, J. BUILD. STRUCT. 37 (01) (2016) 31-40, http://doi.org/10.14006/j.jzjgxb.2016.01.004 [in Chinese]

19 N. Li, J. Qian, L. Ye, et al., Experimental study on seismic behavior of pre-cast shear walls with partial vertical distributed steel bars pressed sleeve splicing, CHINA CIV. ENG. J. 49 (07) (2016) 36-48, http://doi.org/10.15951/j.tmgcxb.2016.07.003 [in Chinese]

20 G. Pan, J. Cai, C. Yang, et al., Experimental study on seismic behavior of precast RC shear walls connected by extruding steel sleeves and rebars. J. BUILD. STRUCT. 42 (05) (2021) 111-120, http://doi.org/10.14006/j.jzjgxb.2020.C034 [in Chinese]

21 B. Wang, L. Yan, Q. Fu, et al., A comprehensive review on recycled aggregate and recycled aggregate concrete, RESOUR. CONSERV. RECY. 171 (2021) 105565, http://doi.org/10.1016/j.resconrec.2021.105565

22 T. Pavlů, K. Fořtová, D. Mariaková, et al., High-performance concrete with fine recycled concrete aggregate: Experimental assessment, Structural Concrete. (2022), https://doi.org/10.1002/suco.202200734

23 B. Liu, C. Feng, Z. Deng, Shear behavior of three types of recycled aggregate concrete, Constr. Build. Mater. 217 (2019) 557-572, http://doi.org/10.1016/j.conbuildmat.2019.05.079

24 R.V. Silva, J. de Brito, R.K. Dhir, Establishing a relationship between modulus of elasticity and compressive strength of recycled aggregate concrete, J. Clean. Prod. 112 (2016) 2171-2186, http://doi.org/10.1016/j.jclepro.2015.10.064

25 S. Marinković, I. Josa, S. Braymand, et al., Sustainability assessment of recycled aggregate concrete structures: A critical view on the current state-of-knowledge and practice, Structural Concrete. (2023) https://doi.org/10.1002/suco.202201245

26 Ministry of Housing and Urban-Rural Development of the People's Republic of China, Technical specification for Concrete Structures of Tall Building, JGJ 3-2010, Beijing, China, 2010. [in Chinese]

27 Ministry of Housing and Urban-Rural Development of the People's Republic of China, Code for Design of Concrete Structures, GB 50010-2010, Beijing, China, 2010. [in Chinese]

28 General Administration of Quality Supervision, Inspection and Quarantine of the People's Republic of China, Recycled Fine Aggregate for Concrete and Mortar, GB/T 25176-2010, Beijing, China, 2010. [in Chinese]

29 Ministry of Housing and Urban-Rural Development of the People's Republic of China, Technical Specification for Application of Recycled Aggregate, JGJ/T 240-2011, Beijing, China, 2011. [in Chinese]

30 Ministry of Housing and Urban-Rural Development of the People's Republic of China, Code for Recycling of Construction & Demolition Waste, GB/T 50743-2012, Beijing, China, 2012. [in Chinese]

31 General Administration of Quality Supervision, Inspection and Quarantine of the People's Republic of China, Quality Carbon Structure Steels, GB/T 699-2015, Beijing, China, 2015. [in Chinese]

32 Ministry of Housing and Urban-Rural Development of the People’s Republic of China, Technical Specification for Mechanical Splicing of Steel Reinforcing Bars, JGJ 107-2016, Beijing, China, 2016. [in Chinese]

33 R. Park, Evaluation of ductility of structures and structural assemblages from laboratory testing, Bull. N. Z. Soc. Earthq. Eng. 22 (3) (1989) 155–166, https://doi.org/10.5459/bnzsee.22.3.155-166

34 Ministry of Housing and Urban-Rural Development of the People’s Republic of China, Specification for Seismic Test of Buildings, JGJ/T 101-2015; Beijing, China, 2015. [in Chinese]

35 Y. Zhang, G. Yuan, Q. Shu, et al. Investigation on seismic behavior of RC shear walls with multiple post-construction openings based on experiment and simulation, J. Build. Eng. 46 (2022) 103707, https://doi.org/10.1016/j.jobe.2021.103707

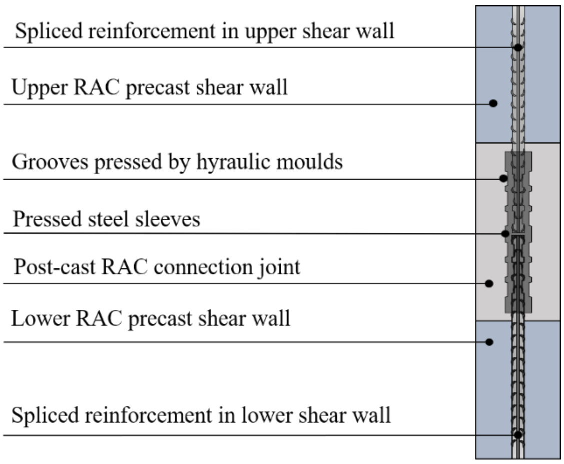

Figure 1 Specifications for the pressed sleeve connection

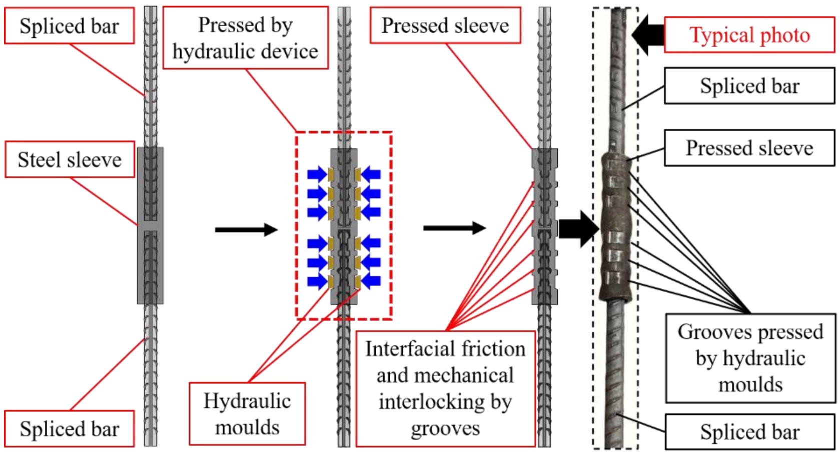

Figure 2 Procedure of using the pressed sleeve to connect two separated bars splices

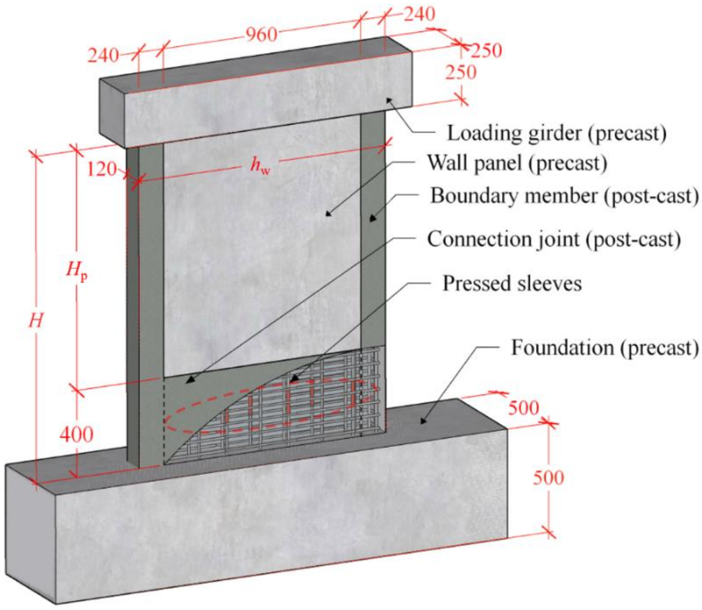

Figure 3 Configurations of the precast specimens (unit. mm)

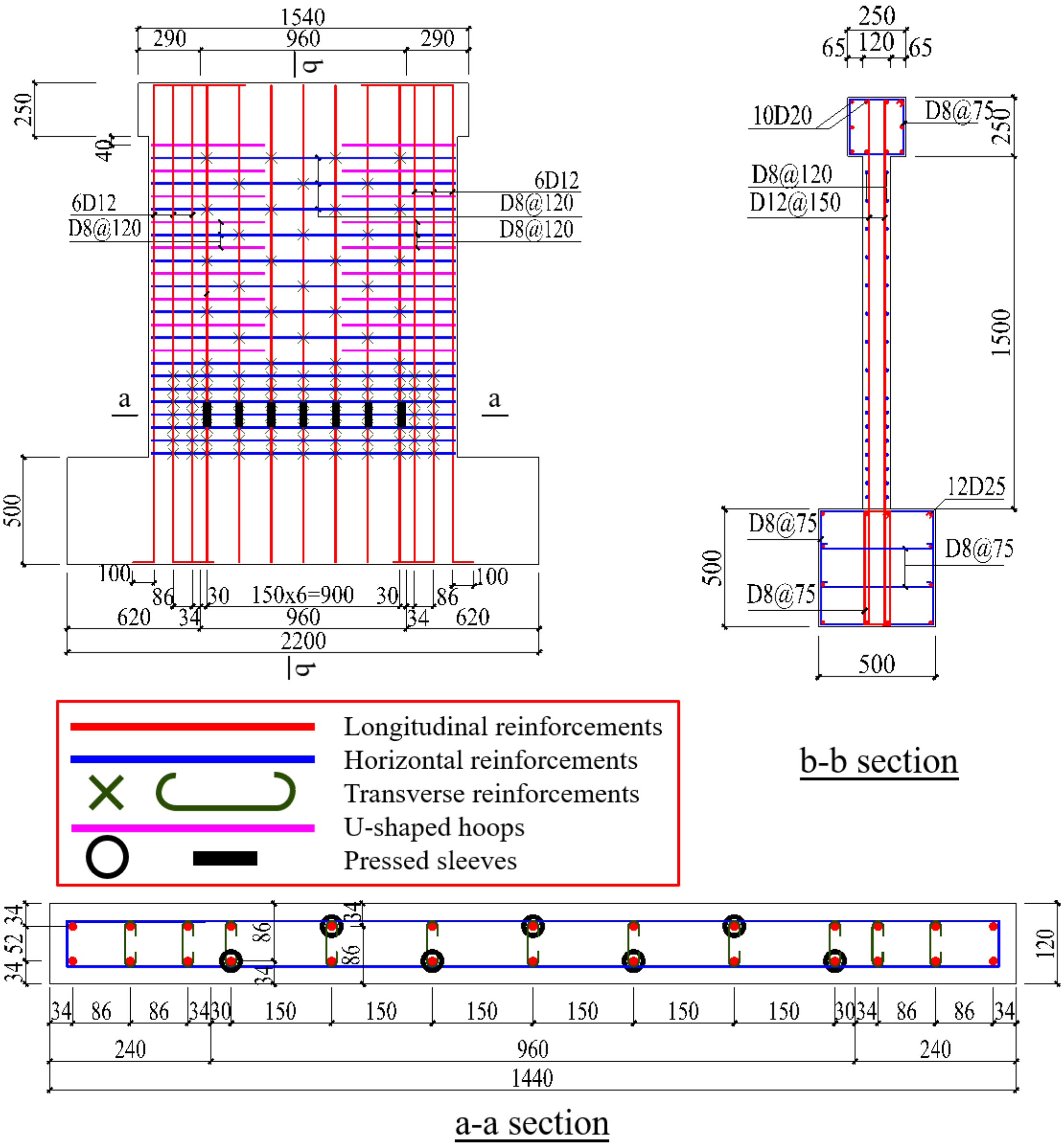

Figure 4 Reinforcement layout for specimens (unit. mm)

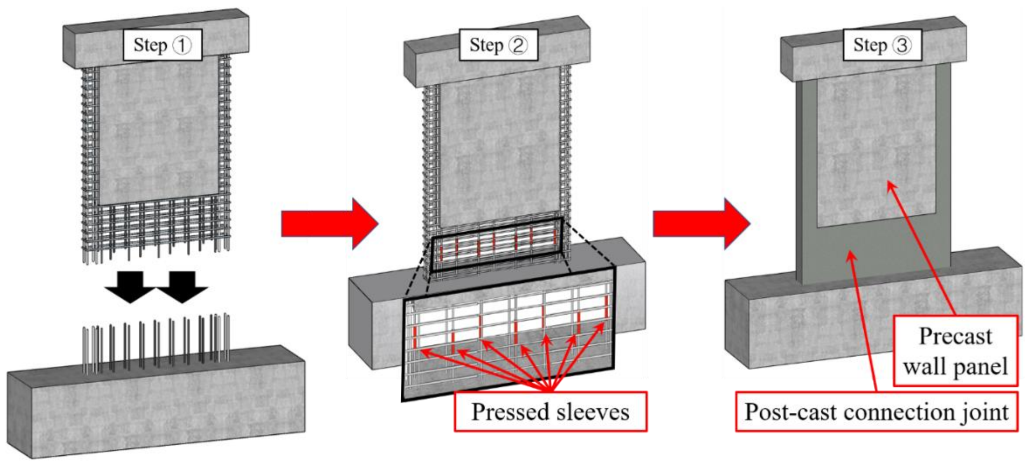

Figure 5 The assembly process of precast specimens

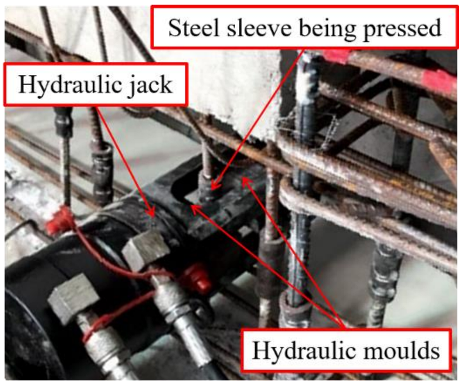

(a) Pressing sleeves on the reinforcements

(b) Pressing device

Figure 6 The process of pressing sleeves

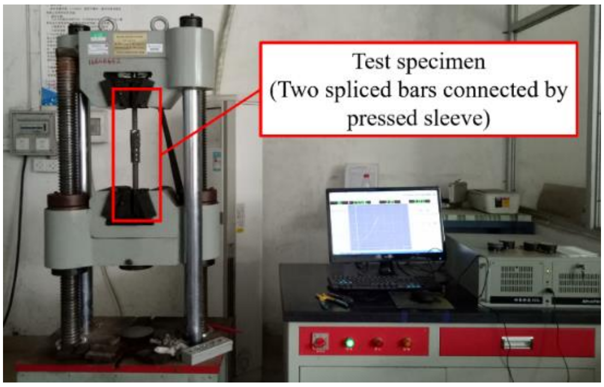

Figure 7 Test of pressed sleeves

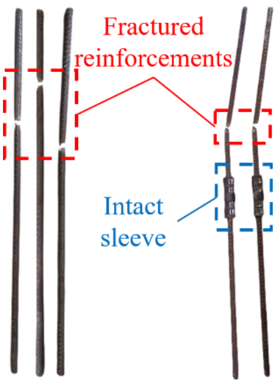

(a) Failure modes

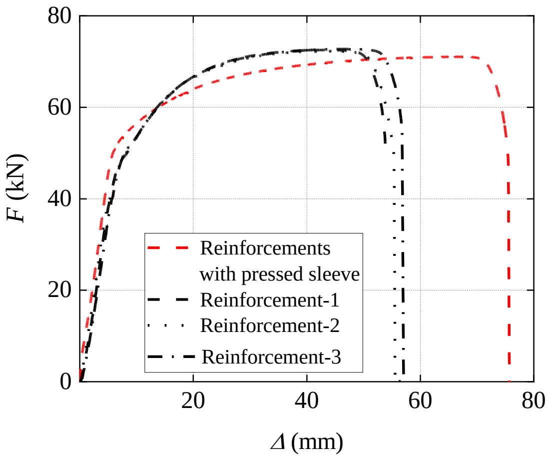

(b) Force–displacement curves

Figure 8 Force–displacement curves and failure modes of sleeve connections (Φ12) and reinforcements (D12)

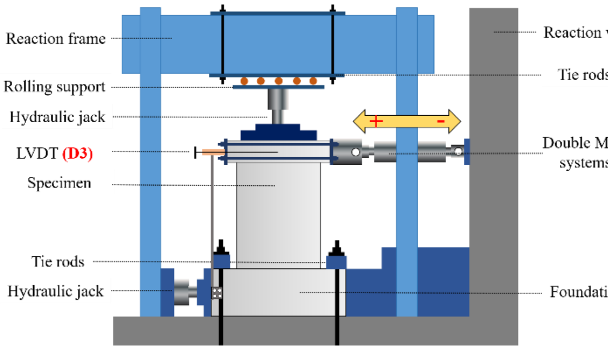

(a) Schematic diagram (front side)

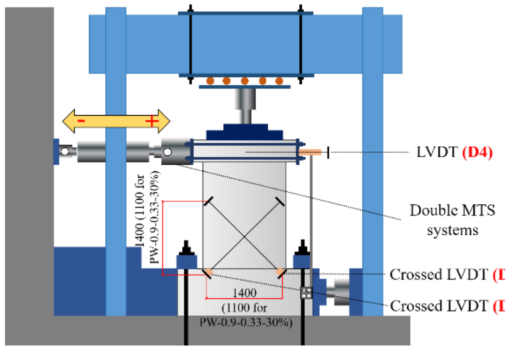

(b) Schematic diagram (back side)

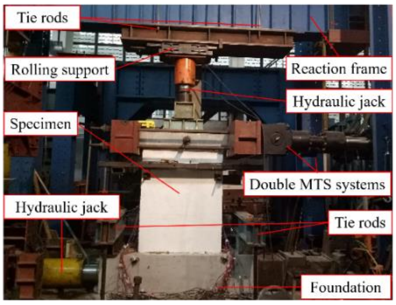

(c) Typical photograph

Figure 9 Test setup (unit. mm)

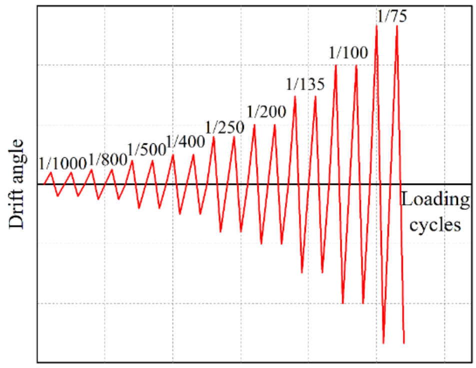

Figure 10 Spectrum of cyclic loading

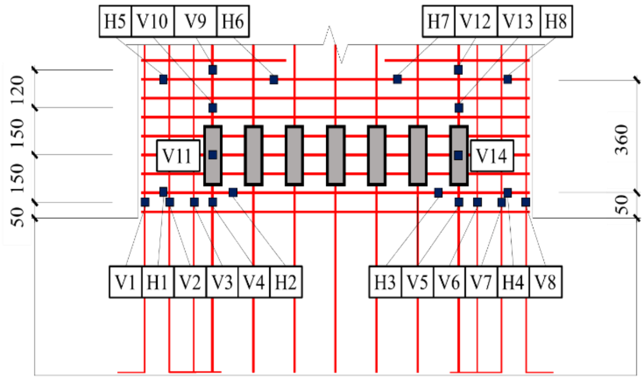

Figure 11 Placement of strain gauges (unit. mm)

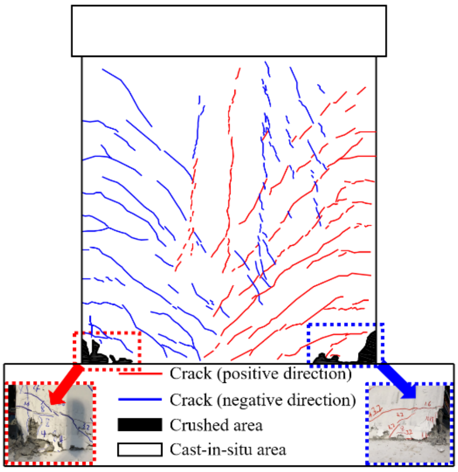

(a) SW-1.1-0.33-30%

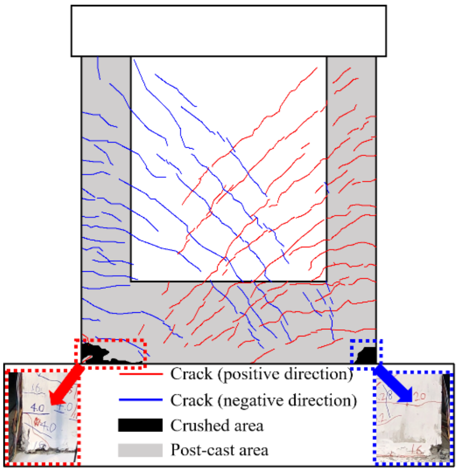

(b) PW-1.1-0.33-30%

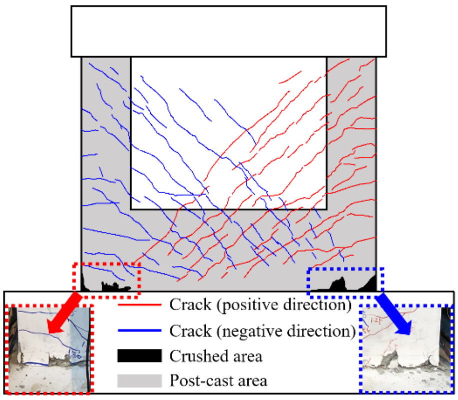

(c) PW-0.9-0.33-30%

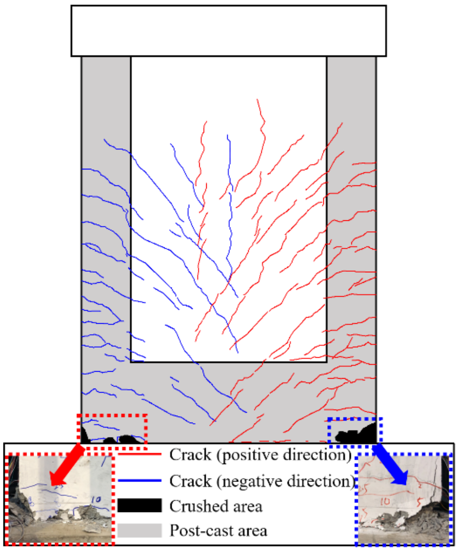

(d) PW-1.4-0.33-30%

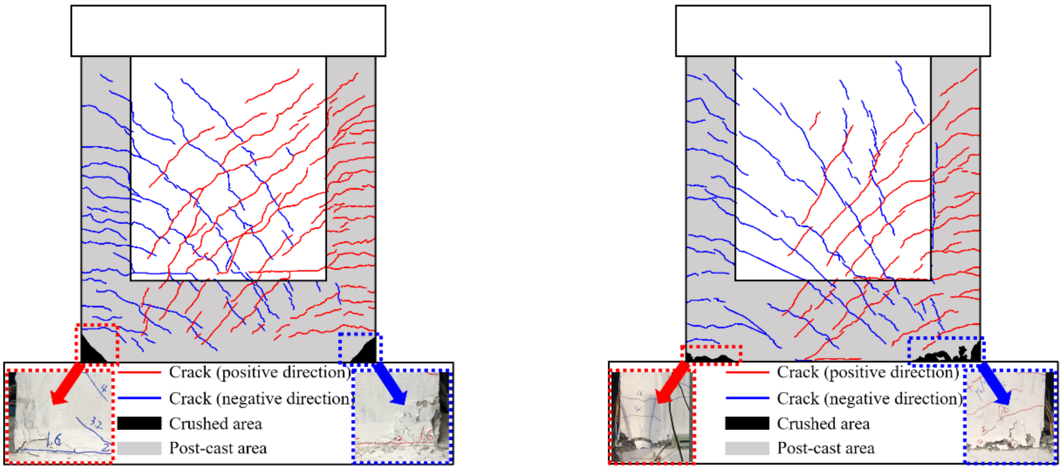

(e) PW-1.1-0.45-30%

(f) PW-1.1-0.20-30%

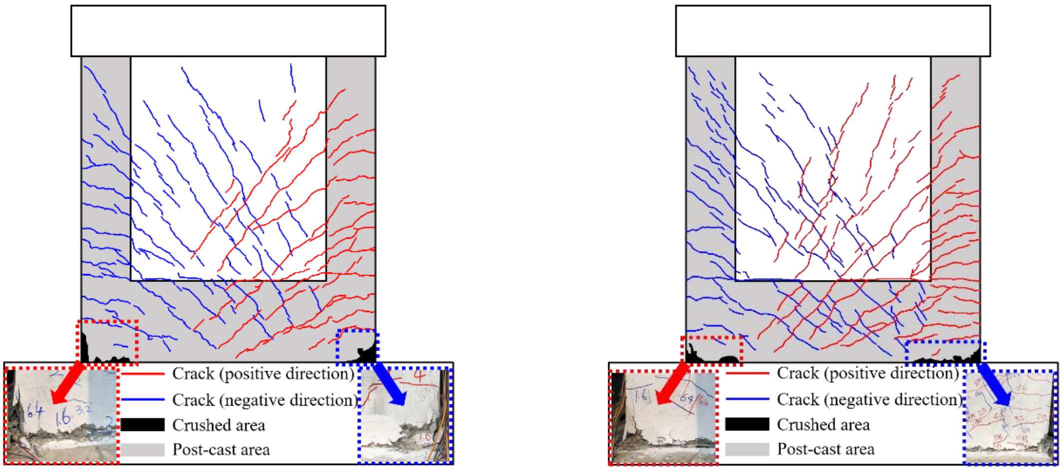

(g) PW-1.1-0.33-0

(h) PW-1.1-0.33-70%

Figure 12 Crack pattern of specimens

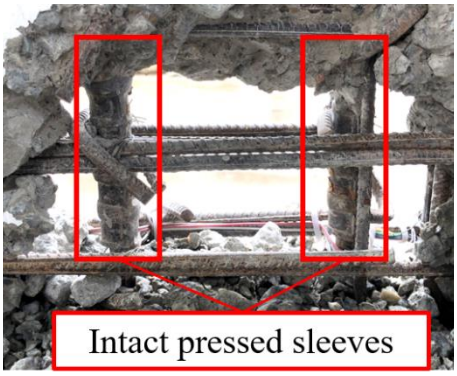

Figure 13 Intact pressed sleeves after cyclic loading test (PW-1.1-0.33-30%)

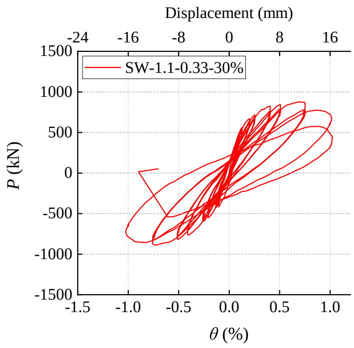

(a) SW-1.1-0.33-30%

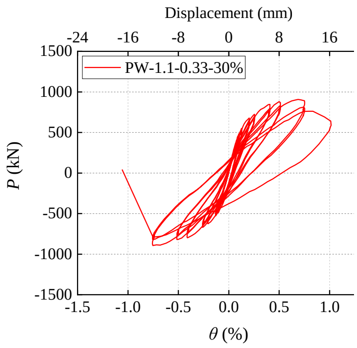

(b) PW-1.1-0.33-30%

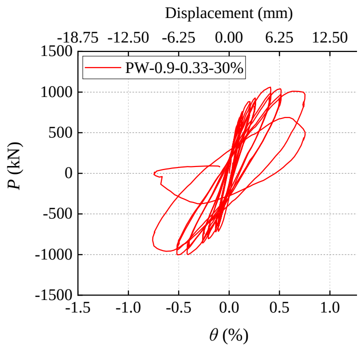

(c) PW-0.9-0.33-30%

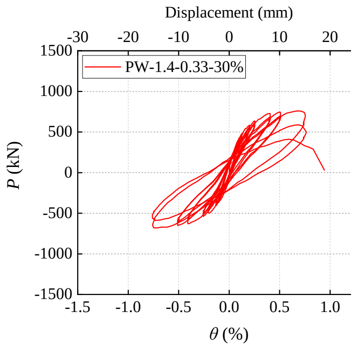

(d) PW-1.4-0.33-30%

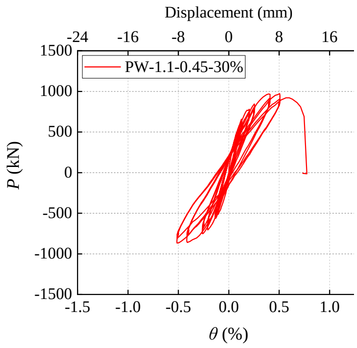

(e) PW-1.1-0.45-30%

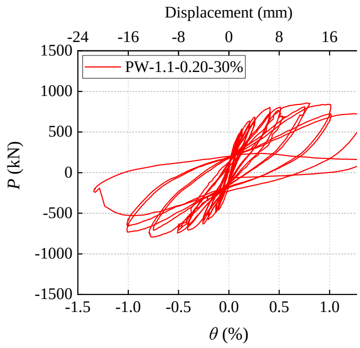

(f) PW-1.1-0.20-30%

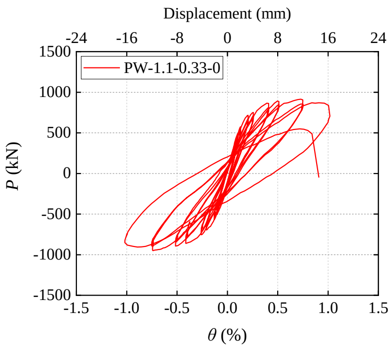

(g) PW-1.1-0.33-0

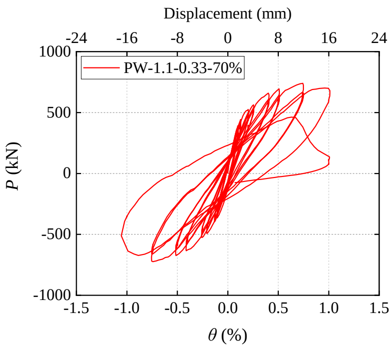

(h) PW-1.1-0.33-70%

Figure 14 Hysteresis curves

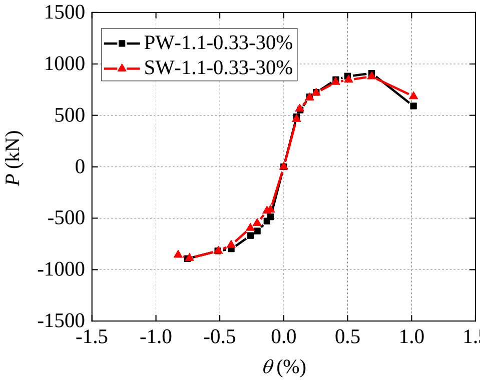

(a) Comparison of precast and cast-in-situ specimens

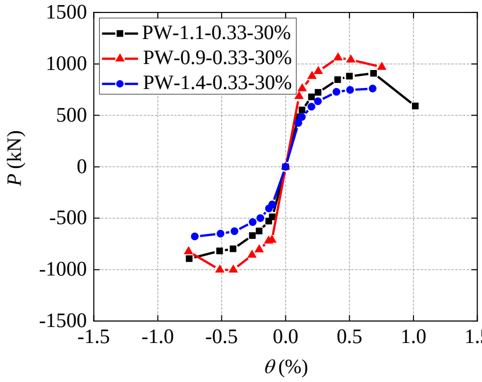

(b) Comparison of specimens with different aspect ratio

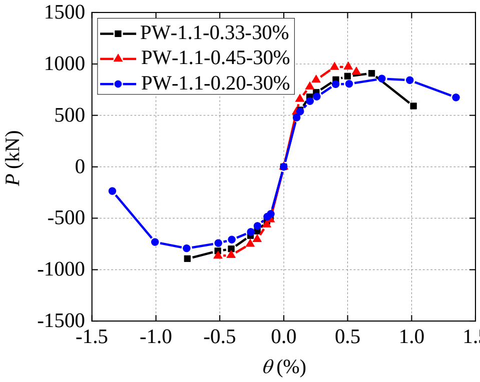

(c) Comparison of specimens with different axial compression ratio

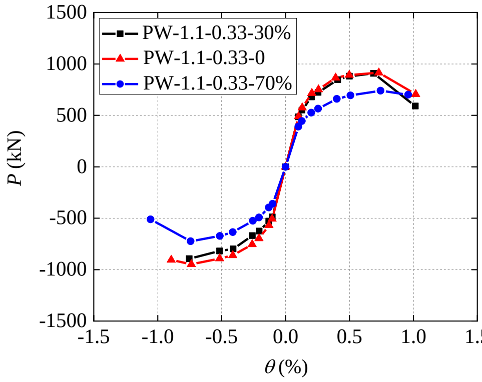

(d) Comparison of specimens with different RFA content

Figure 15 Skeleton curves

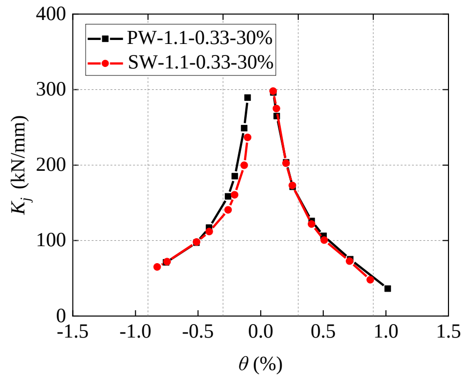

(a) Comparison of precast and cast-in-situ specimens

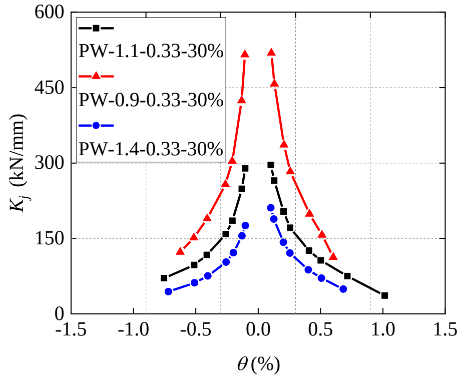

(b) Comparison of specimens with different aspect ratio

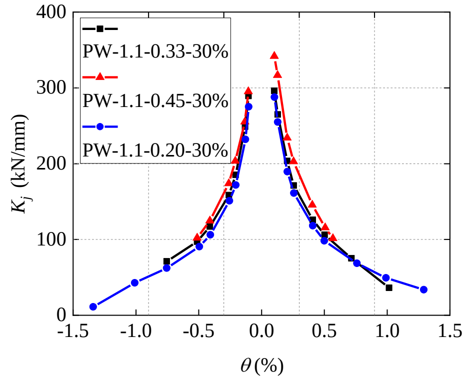

(c) Comparison of specimens with different axial compression ratio

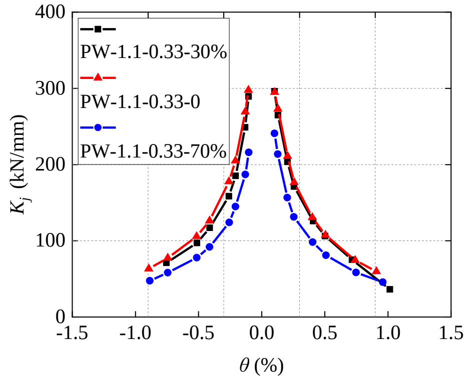

(d) Comparison of specimens with different RFA content

Figure 16 Secant stiffness–drift angle curves

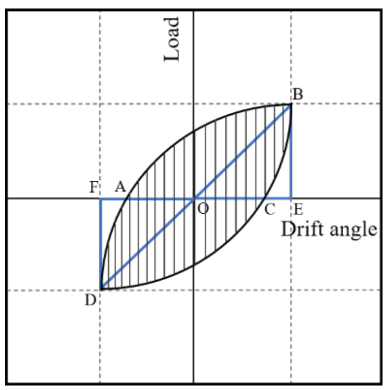

Figure 17 Typical hysteresis loop diagram

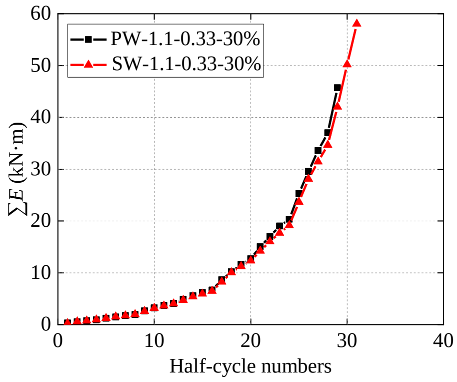

(a) Comparison of precast and cast-in-situ specimens

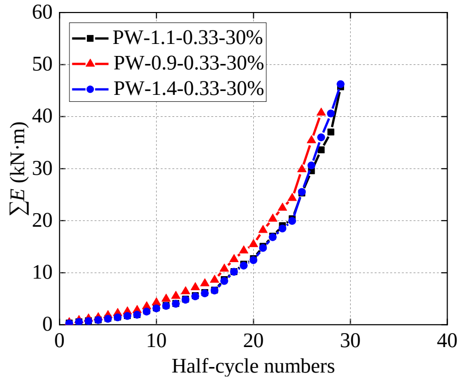

(b) Comparison of specimens with different aspect ratio

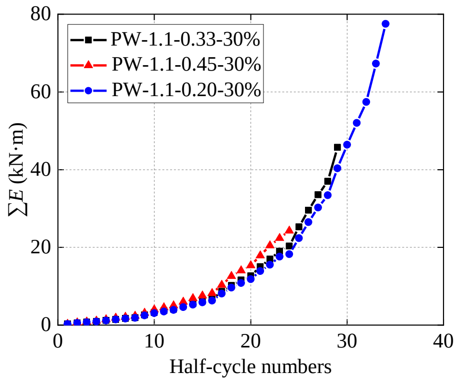

(c) Comparison of specimens with different axial compression ratio

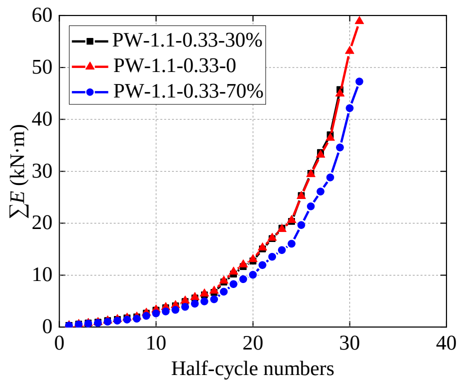

(d) Comparison of specimens with different RFA content

Figure 18 Cumulative dissipated energy

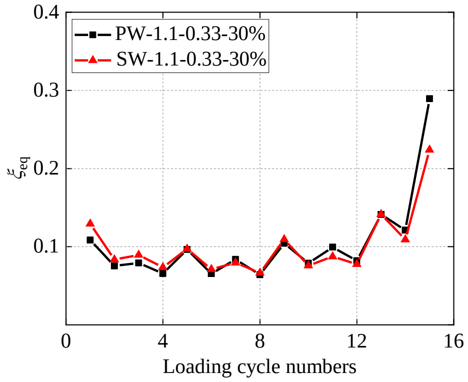

(a) Comparison of precast and cast-in-situ specimens

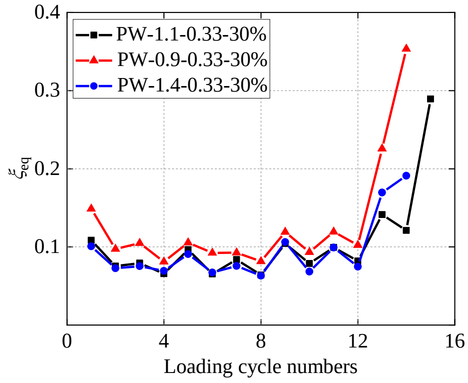

(b) Comparison of specimens with different aspect ratio

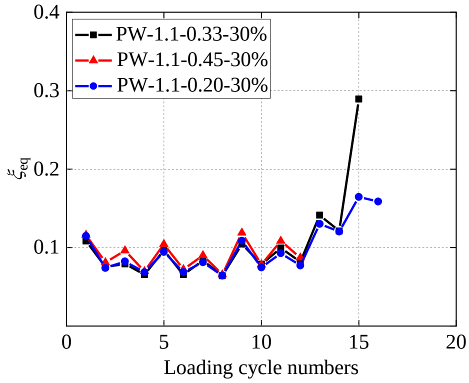

(c) Comparison of specimens with different axial compression ratio

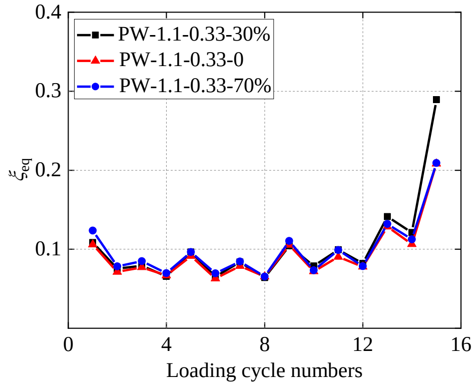

(d) Comparison of specimens with different RFA content

Figure 19 Equivalent viscous damping factor

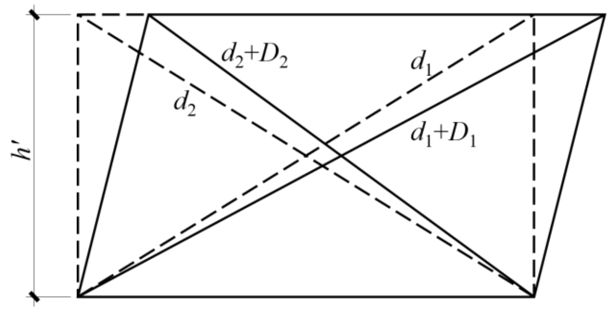

Figure 20 Calculation of the shear distortion

627

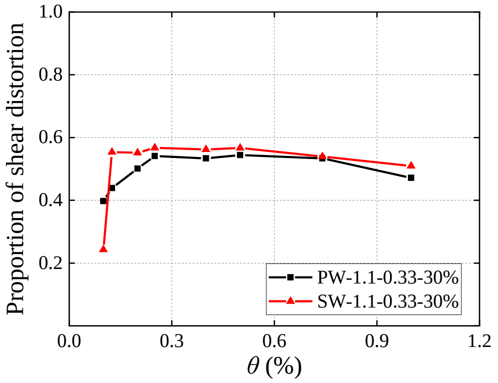

(a) Comparison of precast and cast-in-situ specimens

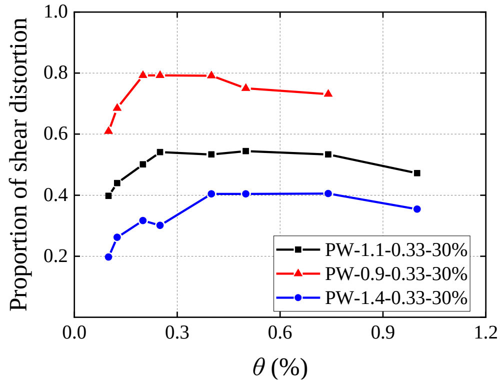

(b) Comparison of specimens with different aspect ratio

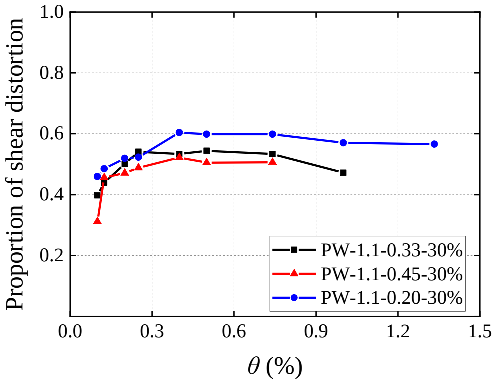

(c) Comparison of specimens with different axial compression ratio

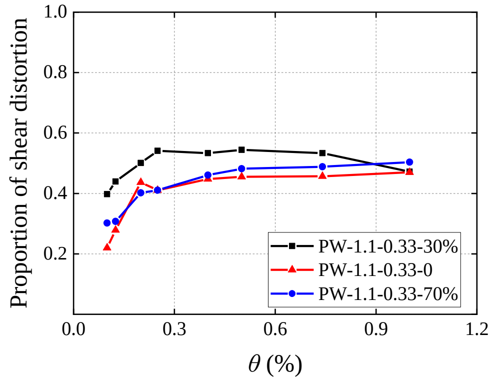

(d) Comparison of specimens with different RFA content

Figure 21 The proportion of shear distortion

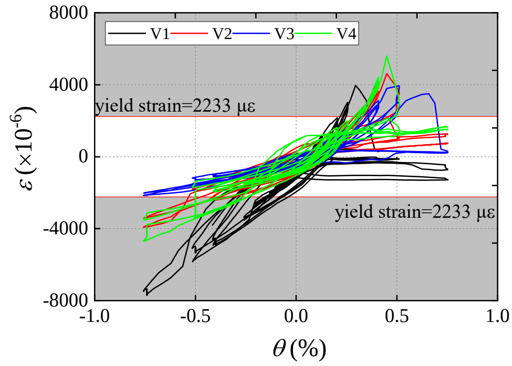

(a) Strains of longitudinal reinforcements measured by V1, V2, V3 and V4

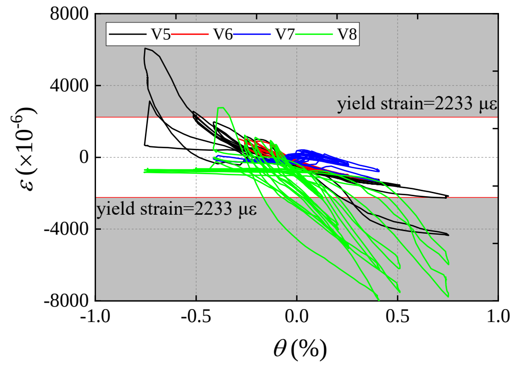

(b) Strains of longitudinal reinforcements measured by V5, V6, V7 and V8

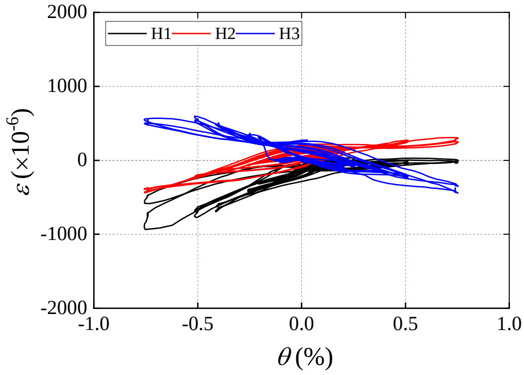

(c) Strains of stirrups measured by H1, H2 and H3

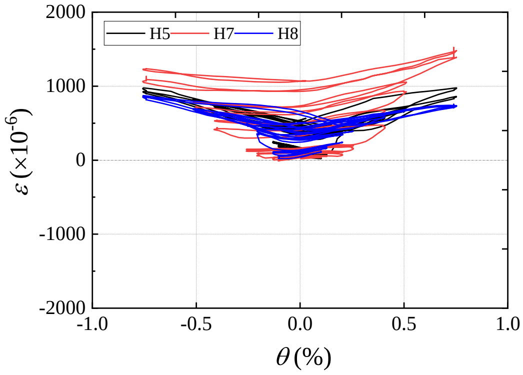

(d) Strains of stirrups measured by H5, H7 and H8

Figure 22 Strains of reinforcements in PW-1.1-0.33-30%

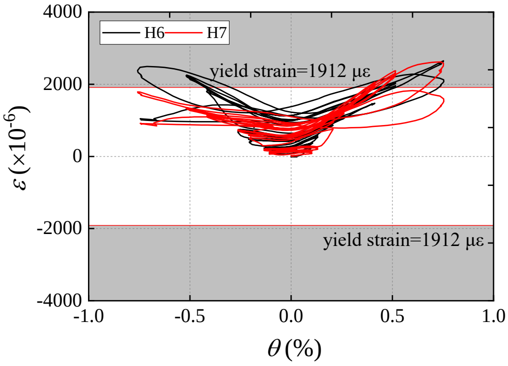

Figure 23 Strains of horizontal reinforcements in PW-0.9-0.33-30%

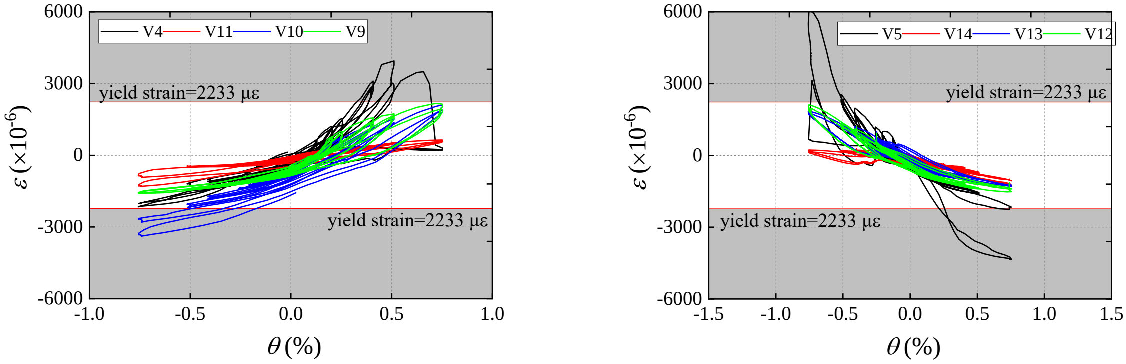

(a) Strains of the pressed sleeve V11 and the connected reinforcement V4, V10 and V9

(b) Strains of the pressed sleeve V14 and the connected reinforcement V5, V12, and V13

Figure 24 Strains of pressed sleeve connections in PW-1.1-0.33-30%

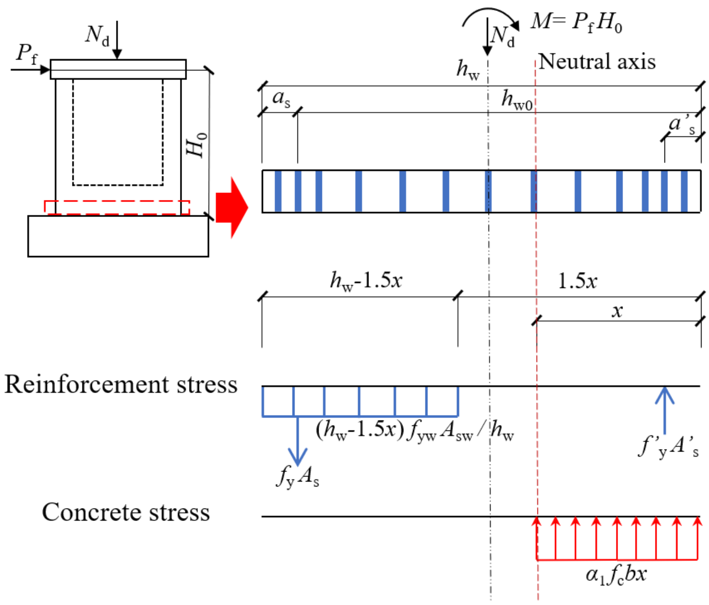

Figure 25 Schematic diagram for calculating flexural strengths

Table 1 Parameters of the specimens.

Specimen label	ω (%)	H_p (mm)	H (mm)	N_d (kN)	n_d	λ	Connection types of longitudinal reinforcements	
							Boundary members	Wall panel
SW-1.1-0.33-30%	30	1100	1500	1738	0.33	1.1	Continuous	Continuous
PW-1.1-0.33-30%	30	1100	1500	1621	0.33	1.1	Lap splice	Pressed sleeves and Lap splice

PW-0.9-0.33-30%	30	750	1150	1621	0.33	0.9	Lap splice	Pressed sleeves and Lap splice
PW-1.4-0.33-30%	30	1500	1900	1621	0.33	1.4	Lap splice	Pressed sleeves and Lap splice
PW-1.1-0.45-30%	30	1100	1500	2210	0.45	1.1	Lap splice	Pressed sleeves and Lap splice
PW-1.1-0.20-30%	30	1100	1500	982	0.20	1.1	Lap splice	Pressed sleeves and Lap splice
PW-1.1-0.33-0	0	1100	1500	1644	0.33	1.1	Lap splice	Pressed sleeves and Lap splice
PW-1.1-0.33-70%	70	1100	1500	1166	0.33	1.1	Lap splice	Pressed sleeves and Lap splice

Table 2 The physical properties of RFA.

	Crush index	Water absorption (%)	Slit content (%)	Cumulative sieve residue (%)						
				4.75mm	2.36mm	1.18mm	0.60mm	0.30mm	0.15mm	0.075mm
RFA	2.7	6.4	6.7	11.9	32.4	49.3	58.1	72.8	85.9	92.9

Table 3 The mix proportions of concrete.

RFA content	RFA (kg/m^3)	Sand (kg/m^3)	Coarse aggregate (kg/m^3)	Cement (kg/m^3)	Coal ash (kg/m^3)	Water (kg/m^3)

0%	0	698	1138	338	38	194
30%	209	489	1138	338	38	205
70%	489	209	1138	338	38	219

Table 4 Concrete strengths of the specimens.

Specimen label	Precast wall panel					Post-cast concrete				
	α (%)	f_{cu} (MPa)	f_c (MPa)	f_t (MPa)	E_c (MPa)	α (%)	f_{cu} (MPa)	f_c (MPa)	f_t (MPa)	E_c (MPa)
SW-1.1-0.33-30%	30	40.1	30.4	3.0	23306	–	—	—	—	—
PW-1.1-0.33-30%	30	38.1	29.0	2.9	25957	30	37.4	28.4	2.9	25825
PW-0.9-0.33-30%	30	39.6	30.1	3.0	26223	30	37.4	28.4	2.9	25825
PW-1.4-0.33-30%	30	37.2	28.3	2.9	2578	30	37.4	28.4	2.9	2582

PW-1.1-0.45-30%	30	38.1	29.0	2.9	72595	30	37.4	28.4	2.9	52582
PW-1.1-0.20-30%	30	38.1	29.0	2.9	72595	30	37.4	28.4	2.9	52582
PW-1.1-0.33-0	0	41.2	31.3	3.1	73286	0	37.9	28.8	2.9	53210
PW-1.1-0.33-70%	70	33.2	25.2	2.7	324951	70	26.9	20.4	2.4	523306

Table 5 Material properties of reinforcements.

Symbol	Diameter (mm)	f_y (MPa)	f_u (MPa)	E_s (GPa)	Type and grade
D8	8	415	640	217	HRB400
D12	12	422	644	189	HRB400

Table 6 Details of pressed sleeves.

Type	Inner diameter (mm)	Outer diameter (mm)	Thickness (mm)	Length (mm)	Recommended extrusion pressure (MPa)
Φ12	16	24	4	100	38-40

Table 7 The key test results and ductility coefficients of specimens.

Specimen label	Lateral direction	P_y (kN)	θ_y	P_m (kN)	θ_m	P_u (kN)	θ_u	μ
SW-1.1-0.33-30%	+	720.2	1/390	877.3	1/145	745.5	1/110	3.6
	-	774.3	1/232	888.8	1/136	755.7	1/103	2.3
PW-1.1-0.33-30%	+	738.8	1/364	907.0	1/145	771.0	1/120	3.0
	-	744.0	1/291	894.3	1/132	894.3	>1/132	>2.2
PW-0.9-0.33-30%	+	875.7	1/391	1059.5	1/245	969.5	>1/133	>2.9
	-	8	1	10	1	8	1/1	3

		11.9	/463	02.2	/245	52.6	39	.3
PW-1.4-0.33-30%	+	636.6	1/392	759.1	1/147	703.9	>1/132	>3.0
	-	554.5	1/357	679.3	1/141	653.4	>1/132	>2.7
PW-1.1-0.45-30%	+	812.7	1/432	971.8	1/198	921.9	>1/176	>2.5
	-	732.0	1/421	867.0	1/195	849.9	>1/195	>2.2
PW-1.1-0.20-30%	+	701.9	1/356	856.6	1/130	728.5	1/81	4.4
	-	652.8	1/340	793.8	1/132	674.9	1/96	3.6
PW-1.1-0.33-0	+	747.6	1/390	914.2	1/137	776.9	1/109	3.6
	-	7	1	94	1	8	>1/	>

		78.36	/3401	9.2	/1361	51.36	98	3.5
PW-1.1-0.33-70%	+	07.86	/3081	739.5	/1341	80.06	>1/99	>3.1
	-	08.1	/267	724.3	/134	15.4	1/111	2.4

Note: The symbol “>” means that the lateral maximum displacement corresponding to the specimen was heavily damaged and incapable for a 15% strength degradation from the peak load P_m.

Table 8 Comparisons of strength predictions against test results.

Specimen label	Loading direction	P_m (kN)	P_{avg} (kN)	V_{sl} (kN)	V_s (kN)	P_f (kN)	P_f/P_{avg}	Failure mode
SW-1.1-0.33-30%	+	877.3	883.1	2135.6	1099.6	837.9	0.95	FC
	-	888.8						
PW-1.1-0.33-30%	+	907.0	900.7	2042.0	1016.8	812.2	0.90	FC
	-	894.3						

PW-0.9-0.33-30%	+	1059.5	1030.9	2042.0	1016.8	1039.6	1.01	FS
	-	1002.2						
PW-1.4-0.33-30%	+	759.1	719.2	2042.0	1016.8	649.7	0.90	FC
	-	679.3						
PW-1.1-0.45-30%	+	971.8	919.4	2513.2	1016.8	825.8	0.90	FC
	-	867.0						
PW-1.1-0.20-30%	+	856.6	825.2	1530.8	1016.8	732.6	0.89	FC
	-	793.8						
PW-1.1-0.33-0	+	914.2	931.7	2060.4	1019.7	817.6	0.88	FC
	-	949.2						
PW-1.1-0.33-70%	+	739.5	731.9	1678.0	958.8	666.5	0.91	FC
	-	724.3						
						MEAN	0.92	
						COV	0.05	

Note: FC represents the flexure-compression failure mode, FS represents the flexure-shear failure mode.

36